Solitary attractors and low-order filamentation in anisotropic self-focusing media

A. A. Zozulya and D. Z. Anderson
JILA, University of Colorado, Boulder, Colorado 80309-0440

A. V. Mamaev* and M. Saffman
Optics and Fluid Dynamics Department, Risø National Laboratory, Postbox 49, DK-4000 Roskilde, Denmark
(Received 5 March 1997)

We present a detailed theoretical analysis of the properties and formation of single solitons and higher-order bound dipole pairs in media with anisotropic nonlocal photorefractive material response. The single solitons are elliptical beams, whereas the dipole pairs are formed by a pair of displaced elliptical beams with a π phase shift between their fields. The theory predicts convergence of Gaussian beams to the solitary states within a certain basin of attraction. Experimental observation of these solitons has been presented elsewhere. The experimental portion of the present paper concentrates on the region further away in parameter space, where complex spatial oscillations, including asymmetric filamentation into several beamlets, occurs.
[S1050-2947(97)03011-4]

PACS number(s): 42.65.Tg, 42.50.Jx, 42.65.Hw

I. INTRODUCTION

The possibility of creating two-transverse-dimensional $[(2+1)\mathrm{D}]$ soliton-type structures of light in nonlinear media is of considerable interest due to potential applications in optical information processing systems [1]. The dynamics of nonlinear propagation equations resulting in the formation of such structures can be very complex and may result in the generation of higher-order and multisoliton solutions. These solutions have been investigated extensively in the $(1+1)$D (one-transverse-dimensional) case [2], where a number of exact analytical methods have been developed including the inverse scattering method, which provides an exact solution of an initial-value problem, Bäcklund transformations, and Lax pairs. Examples of higher-order bound soliton solutions include the formation of soliton-antisoliton pairs (kinks) [3], incoherently coupled bright and dark beams [4], and multisoliton solutions of a set of coupled high-order nonlinear Schrödinger equations [5]. The existence and properties of higher-order and multisoliton solutions in the $(2+1)$D case have been investigated much less than in the $(1+1)$D case. Noteworthy results include calculation of nonlinear dipolar structures in the context of the Korteweg–de Vries equation [6], molecular matrices with impurities [7], and fluids [8]. Higher-order radially symmetric structures in media with cubic nonlinearity were given in Ref. [9], and their evolution in a saturating nonlinear medium was studied in Ref. [10]. More complex localized solutions were described in Ref. [11].

In this paper we present a detailed theory addressing properties and formation of $(2+1)$D (two-transverse-dimensional) solitons in media with a photorefractive optical nonlinearity. Self-focusing in photorefractive media was first studied experimentally several years ago [12,13], and this is presently a very active topic [14–16]. The possibility of obtaining large optical nonlinearities using low-power continuous-wave lasers has made photorefractive materials attractive for studying a range of spatial dynamics including modulation instabilities [17,18], vortex dynamics [19], generation of spatial subharmonics [20], and pattern formation [21].

Photorefractive materials respond to the presence of the optical field $B(\vec{r})$ by a nonlinear change in the refractive index δn that is both an anisotropic and nonlocal function of the light intensity. The anisotropy does not allow radially symmetric soliton solutions thereby necessitating explicit treatment of both transverse coordinates. The nonlocality is another feature of the photorefractive response that makes it significantly different from typical nonlinear optical media, where the refractive index δn is an algebraic (local) function of the light intensity. This local response in the simplest case $\delta n \propto |B|^2$ results in the canonical nonlinear Schrödinger equation for the amplitude of light propagating in the medium [22]. Higher-order nonlinearities result in various forms of local saturable response [23]. In photorefractive media the change in the refractive index is proportional to the amplitude of the static electric field induced by the optical beam. Finding the material response therefore requires solving an elliptic-type equation for an electrostatic potential with a source term due to light-induced generation of mobile carriers. The corresponding elliptic boundary-value problem has to be treated globally in the whole volume of the nonlinear medium. An immediate consequence of this fact is that both single and multisoliton $(2+1)$D solitary solutions in photorefractive media have exponential asymptotics for the electromagnetic field, but algebraic asymptotics for the nonlinear refractive index of the medium, and in this sense can be called semialgebraic. The reason is that the above electrostatic potential is that of a two-dimensional distributed induced dipole, and has algebraic tails even for an exponentially localized beam. Note that typical soliton solutions of nonlinear propagation equations have exponentially decaying asymptotics at infinity. Several notable exceptions include

*Permanent address: Institute for Problems in Mechanics, Russian Academy of Sciences, Prospekt Vernadskogo 101, Moscow, 117526 Russia.

 © 1998 The American Physical Society

solutions of the Benjamin-Ohno equation (for a recent review see, e.g., Ref. [24]) or the *K-P* equation [25] that are algebraic in nature.

Due to the above circumstances the equations governing propagation of a light beam in focusing and/or defocusing photorefractive media [26,27] have no direct analogs in nonlinear optics. Their closest structurally similar counterparts probably are Davey-Stewartson equations [28] describing nonlinear dispersive waves in fluid dynamics, or Zakharov equations for parametrically coupled electromagnetic and Langmuir waves in plasmas [29].

The paper is organized as follows. In Sec. II we discuss the structure of the basic set of equations describing self-focusing of a light beam in photorefractive media. Three complementary techniques are used to study solutions of these equations. First, in Sec. II A, we give an approximate analytical solution describing evolution of a single light beam in the aberrationless approximation. The solution demonstrates the possibility of the existence of soliton solutions. The analytical solution is obtained in the limit of weak saturation of the nonlinear response. For arbitrary values of the saturation we use the exact numerical procedure described in Sec. II B to construct soliton solutions. These solutions are found and their properties analyzed in detail, in Sec. III. In the weak saturation limit the analytical and numerical procedures lead to soliton profiles that agree within the limits of the approximations used. In order to address the question of convergence of arbitrary Gaussian beams to the soliton asymptotic states, the value of the convergence rate, and its dependence on the parameters of the problem, we solve the basic equations (2) numerically. The answers determine whether the soliton solutions can be obseved in experiment, and outline the region of parameters where the convergence takes place. These numerical results are given in the latter part of Sec. III.

Section IV repeats the analysis of Sec. III for higher-order bound dipole soliton pairs. Gaussian beams lying outside the basin of attraction of the above soliton solutions exhibit complex spatial dynamics. For large beams an order of magnitude or more wider than the soliton solutions, filamentation occurs [30], resulting in a spatially disordered, statistically homogeneous distribution [18]. Beams with parameters relatively close to the soliton solutions exhibit low-order filamentation and split into several child beams. The child beams evolve in a complex fashion with strong oscillations in their energy and relative sizes. Repeated cycles of splitting and fusion may occur. Section V presents numerical and experimental results on these complex dynamics. Finally, Sec. VI is devoted to discussion of the results.

II. GENERAL ANALYSIS

Steady-state propagation of an optical beam $B(\vec{r})$ in a photorefractive medium is governed by the set of equations [26]

$$\left[\frac{\partial}{\partial x}-\frac{i}{2}\nabla^2\right]B(\vec{r})=i\frac{\partial\varphi}{\partial z}B(\vec{r}), \tag{1a}$$

$$\nabla\cdot\left[\frac{1+|B|^2}{1-\zeta\nabla\cdot(\hat{\epsilon}_n\nabla\varphi)}(\nabla\varphi-\vec{e}_z)-\left(\frac{\widetilde{E}}{E_{ext}}\right)^2\zeta\nabla\frac{1+|B|^2}{1-\zeta\nabla\cdot(\hat{\epsilon}_n\nabla\varphi)}\right]=0. \tag{1b}$$

Here $\nabla=\hat{y}(\partial/\partial y)+\hat{z}(\partial/\partial z)$, and φ is the dimensionless electrostatic potential induced by the beam with the boundary conditions $\nabla\varphi(\vec{r}\to\infty)\to 0$. The dimensionless coordinates (x,y,z) are related to the physical coordinates (x',y',z') by the expressions $(y,z)=l_\perp(y',z')$ and $x=kl_\perp^2x'$, where $l_\perp=(kn^2)^{-1}(2/r_{\rm eff}E_{\rm ext})^{1/2}$. Here k is the wave number of light in the medium, n is the index of refraction, $r_{\rm eff}$ is the effective element of the electro-optic tensor, $\widetilde{E}$ is the characteristic value of the internal field, and $E_{\rm ext}$ is the amplitude of the external field directed along the z axis far from the beam. The normalized intensity $|B(\vec{r})|^2$ is measured in units of saturation intensity I_d, so that the physical beam intensity is given by $|B(\vec{r})|^2I_d$. Finally, $\hat{\epsilon}_n$ is the diagonal dielectric tensor of the medium normalized to the value of its component along the z axis ϵ_{33}, and $\zeta=(E_{\rm ext}/\widetilde{E})(1/k_Dl_\perp)$, where k_D is the Debye wave number.

Terms proportional to the parameter ζ in Eq. (1) describe contributions from the antisymmetric part of the photorefractive nonlinearity responsible for beam bending [31,32] and incoherent stimulated scattering. For typical spatial structures of light in the conditions when these terms are dominant, see Ref. [33]. In the region of parameters corresponding to the experimental investigation of photorefractive self-focusing these terms are frequently not important and can be neglected. In this limit $\zeta=0$ and Eqs. (1) take the form ([26,18]).

$$\left[\frac{\partial}{\partial x}-\frac{i}{2}\nabla^2\right]B(\vec{r})=i\frac{\partial\varphi}{\partial z}B(\vec{r}), \tag{2a}$$

$$\nabla^2\varphi+\nabla\ \ln(1+|B|^2)\cdot\nabla\varphi=\frac{\partial}{\partial z}\ln(1+|B|^2). \tag{2b}$$

A. Approximate analytical solutions

The strong anisotropy of Eqs. (2) does not allow radially symmetric solutions [26,27]. In the simplest approximation the beam should be treated as elliptical and characterized by two diameters d_y and d_z along the y and z axes, respectively. Its amplitude in the parabolic approximation can be expressed in the form

$$B=\sqrt{I_m(x)}\ \exp\left[-\frac{4y^2}{d_y^2}-\frac{4z^2}{d_z^2}+i\frac{y^2}{2}\frac{d_y'}{d_y}+i\frac{z^2}{2}\frac{d_z'}{d_z}+i\theta\right], \tag{3}$$

where $I_m(x)=I_{\rm in}d_y(0)d_z(0)/d_yd_z$, $I_{\rm in}$ is the input beam intensity, and $\theta(x)$ is the nonlinear phase change. The primes denote differentiation with respect to x. In the unsaturated regime $I_m\leqslant 1$, Eq. (2b) reduces to $\nabla^2\varphi=\partial|B(\vec{r})|^2/\partial z$. Its solution in cylindrical coordinates $y=r\cos\psi$, $z=r\sin\psi$ takes the forms

$$\varphi(r,\psi)=\frac{I_m}{16d_z^2}\sum_{k=0}^{\infty} r^{2k+1}F_k(r^2)\sin(2k+1)\psi, \quad (4a)$$

$$F_k=\int_{\infty}^{r^2} d\tau\ \tau^{-2k-2}\int_0^{\tau} d\tau'\,\tau'^{k+1}A_k(\tau')\exp(-a\tau'), \quad (4b)$$

$$A_k=(-1)^{k+1}[\delta_{k,0}+(1-\delta_{k,0})I_k(b\tau)+I_{k+1}(b\tau)]. \quad (4c)$$

Here $a=4(d_y^{-2}+d_z^{-2})$, $b=4(d_y^{-2}-d_z^{-2})$, and I_k are modified Bessel functions.

The refractive index in the central region of the beam according to Eqs. (4) is given by the expression

$$\nu(y,z)=-8I_m\frac{d_z^2y^2+(d_y^2+2d_yd_z)z^2}{d_z^2(d_y+d_z)^2}. \quad (5)$$

Substituting expressions (5) and (3) into Eq. (2a), one arrives at the set of equations [36]

$$d_y''=16d_y^{-3}[4-\kappa F^3(F+1)^{-2}], \quad (6a)$$

$$d_z''=16d_z^{-3}[4-\kappa(F+2)(F+1)^{-2}], \quad (6b)$$

where $\kappa=I_{\rm in}d_y(0)d_z(0)$, and $F=d_y(x)/d_z(x)$ is the beam diameter ratio.

Equations (6) demonstrate a nontrivial nonseparable way in which both diameters of the beam contribute to its evolution. In particular they show the possibility of self-channeled propagation $d_y,d_z=\text{const}$ that corresponds to the value of the diameter ratio F determined by the relation $F^3=F+2$ or $F=F_0\approx 1.5$. The self-channeled beam is narrower in the direction of the applied field and wider in the perpendicular direction. The absolute values of the diameters for this case are determined by the relations

$$d_z(0)=2(F_0+1)F_0^{-2}I_{\rm in}^{-1/2}, \quad (7a)$$

$$d_y(0)=2(F_0+1)F_0^{-1}I_{\rm in}^{-1/2}. \quad (7b)$$

Linearizing Eqs. (6) around the self-channeled solution gives the equation for the perturbation of the diameters $\delta d_z(x)=d_z(x)-d_z(0)$ and $\delta d_y(x)=d_y(x)-d_y(0)$

$$\frac{d^2}{dx^2}\delta d_y=-16d_z(0)^{-2}I_{\rm in}\frac{F_0+3}{(F_0+1)^3}(\delta d_y-F_0\delta d_z), \quad (8a)$$

$$\frac{d^2}{dx^2}\delta d_z=16d_z(0)^{-2}I_{\rm in}\frac{F_0(F_0+3)}{(F_0+1)^3}(\delta d_y-F_0\delta d_z). \quad (8b)$$

Four eigenvalues of these equations are

$$\kappa_{1,2}=0, \quad (9a)$$

$$\kappa_{3,4}=\pm i\frac{2I_{\rm in}F_0^2}{(1+F_0)^2}\left(\frac{(F_0+3)(1+F_0^2)}{1+F_0}\right)^{1/2}. \quad (9b)$$

Equations (9) show that the evolution of small perturbations around the self-channeled solution is of an oscillatory nature in the framework of the parabolic approximation. The spatial period of the oscillations is inversely proportional to the intensity of the beam.

B. Exact numerical procedure

The analytical approach indicates the possibility of existence of spatially localized $(2+1)$D soliton solutions of Eqs. (2). They are light beams propagating in the medium without changing their shape: $B(x,y,z)=b(y,z)\exp(i\lambda x)$, where λ is a real propagation constant. The soliton amplitude satisfies the set of equations

$$\left[\lambda-\frac{1}{2}\nabla^2\right]b(y,z)=\frac{\partial\varphi}{\partial z}b, \quad (10a)$$

$$\nabla^2\varphi+\nabla\ \ln(1+|b|^2)\cdot\nabla\varphi=\frac{\partial}{\partial z}\ln(1+|b|^2), \quad (10b)$$

constituting an eigenvalue-eigenfunction problem with the eigenvalues λ forming a continuous set. In the numerical analysis of the eigenproblem (10) we have adopted an approach based on the iterative procedure due to Petviashvili [34] (see also [35,6]).

The basic formula for the iterative process has the form

$$b_{n+1}(\vec{k})=|M|^{-3/2}\frac{\hat{F}[\partial\varphi_n/\partial z b_n(\vec{r})]}{\lambda+k^2/2}, \quad (11)$$

where $\hat{F}$ is the two-dimensional Fourier operator

$$\hat{F}[f(\vec{r})]\equiv f(\vec{k})=\int\int d\vec{r}\ \exp(i\vec{k}\cdot\vec{r})f(\vec{r}), \quad (12)$$

and M is the renormalization parameter ensuring stability of the iterative procedure defined by the relation

$$M=\frac{\int d\vec{k}\ \hat{F}[\partial\varphi_n/\partial z b_n(\vec{r})]b_n^*(\vec{k})}{\int d\vec{k}(\lambda+k^2/2)|b_n(\vec{k})|^2}. \quad (13)$$

The steps of the above iteration scheme are as follows: specify an initial distribution of the field (a starter function) $b_n(\vec{r})$ $(n=0)$, solve Eq. (2b) for $\varphi=\varphi_n(\vec{r})$, calculate the renormalization parameter (13), and compute the next approximation according to Eq. (11). The degree of convergence of the iterative process is controlled by monitoring the norm of the relative error

$$\epsilon=\frac{\int d\vec{r}|b_{n+1}(\vec{r})-b_n(\vec{r})|}{\int d\vec{r}|b_{n+1}(\vec{r})|}\propto\frac{|M-1|}{|M|}. \quad (14)$$

III. SINGLE-BEAM SOLITON SOLUTIONS

The numerical soliton-finding procedure described in Sec. II requires specification of an initial guess $b_0(y,z)$ for the amplitude of the light beam (a starter function). To find single soliton solutions of Eqs. (2), starter functions have been taken to be arbitrary Gaussian beams. The iterations have been carried out until ϵ went below 10^{-4}–10^{-5}. The single-beam soliton solution of Eqs. (2) turns out to be a smooth elliptical beam that is narrower along the coordinate

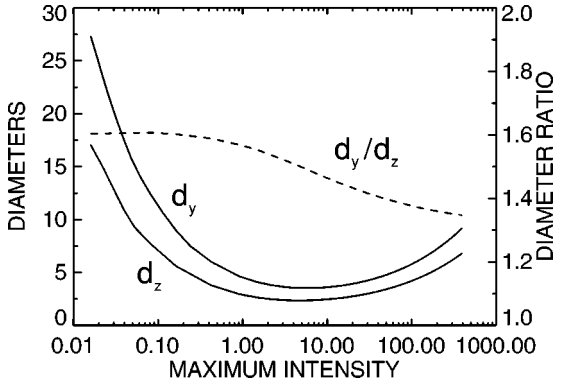

FIG. 1. Diameters of the soliton solution of Eqs. (2) and their ratio vs its maximum intensity.

z (the direction of the applied electric field) and wider in the perpendicular direction. The asymptotic structure of the potential far from the beam is of the form $\varphi \propto z/(y^2+z^2)$. This structure implies that the refractive index $\nu=\partial\varphi/\partial z$ has both positive (focusing) and negative (defocusing) regions; the latter are situated on both sides of the beam along the plus-minus directions of the z axis.

Figure 1 shows the diameters d_y and d_z of the soliton solution and their ratio d_y/d_z as functions of the soliton maximum intensity $I_m=|b(0,0)|^2$. The diameters have been calculated at the $\frac{1}{2}$ level of the maximum intensity. The values of the diameters are inversely proportional to the square root of the soliton maximum intensity $d_{y,z}\propto 1/\sqrt{I_m}$ for $I_m\to 0$, logarithmically proportional to it ($d_{y,z}\propto\sqrt{\ln I_m}$) in the opposite limit $I_m\to\infty$, and pass through shallow minima in between. Notice that the diameter ratio in Fig. 1 is strikingly close to the value $F=1.5$ following from the approximate analytical formulas Eqs. (6). The absolute values of the diameters given by Eqs. (6) are about two times off as compared to exact numerical values in the limit $I_m\ll 1$. The discrepancy between the exact numerical procedure and the approximate analytical solution is due to the Gaussian ansatz made in the analytic development.

The range of soliton maximum intensities in Fig. 1 corresponds to values of the propagation constant λ lying between $\lambda=0.002$ and 0.95. Both the maximum intensity and the power of the soliton are increasing functions of the propagation constant. This is illustrated in Fig. 2, where the soliton maximum intensity versus the propagation constant is shown. Finally, Fig. 3 presents soliton intensity cross sections along the y and z axes for different values of the maximum intensity I_m. The wider profiles are cross sections of the soliton along the y axis and the narrower ones along the z axis. In the unsaturated limit $\lambda\ll 1$ the spatial distribution of the soliton field is universal and does not depend on the value of the propagation constant except for a trivial rescaling. Indeed, in this limit Eq. (2b) reduces to $\nabla^2\nu=\partial^2|B|^2/\partial z^2$, where $\nu=\partial\varphi/\partial z$. The renormalizations $(x,y)=\lambda^{-1/2}(\tilde{x},\tilde{y})$, and $b=\lambda^{1/2}\tilde{b}$, $\nu=\lambda\tilde{\nu}$ transform the eigenvalue-eigenfunction problem for finding the soliton profiles to the universal form

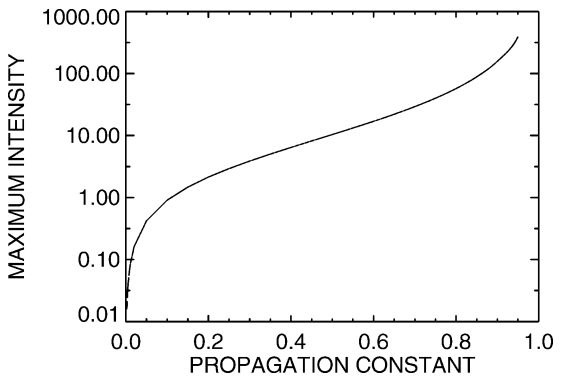

FIG. 2. Soliton maximum intensity vs the propagation constant.

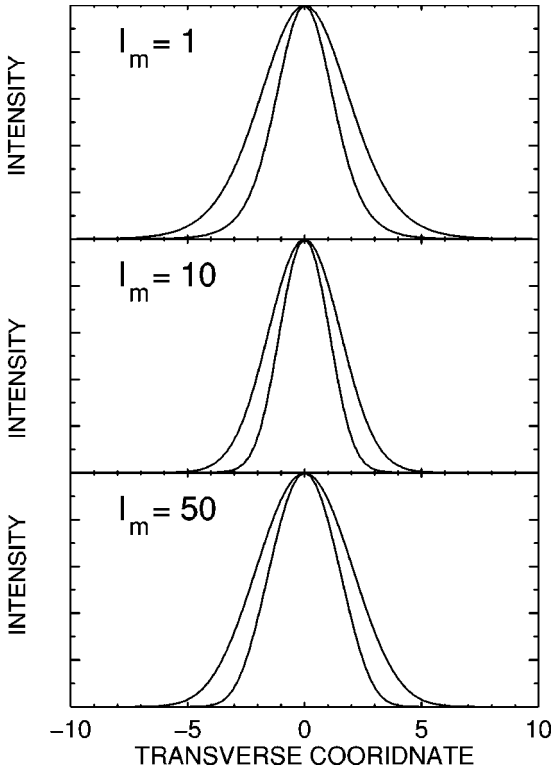

FIG. 3. Soliton intensity cross sections along the y and z axes for $I_m=1$, 10, and 50.

$$[1-\tfrac{1}{2}\tilde{\nabla}^2]\tilde{b}=\tilde{\nu}\tilde{b}, \tag{15a}$$

$$\tilde{\nabla}^2\tilde{\nu}=\frac{\partial^2}{\partial\tilde{z}^2}\,\tilde{b}^2. \tag{15b}$$

Returning to the (x,y) coordinate frame, we immediately conclude that the maximum intensity is proportional to the value of the propagation constant $I_m\propto\lambda$ and the total power $P=\int dx\,dy\,b^2$ is independent of the propagation constant.

Numerical analysis of the evolution of arbitrary initial beams has been carried out by direct numerical solution of the nonlinear propagation equations (2). This analysis shows that the soliton solutions are attractors of the set of equations (2). The rate of convergence to these solutions depends primarily on the normalized intensity I_m. We have found that evolution of an input beam in general is characterized by oscillations of both its diameters, in qualitative agreement with the results of the analytical approach. In the unsaturated limit $I_m\ll 1$ these oscillations are strongly damped, and their spatial period scales as $1/I_m$. Increasing I_m up to about unity

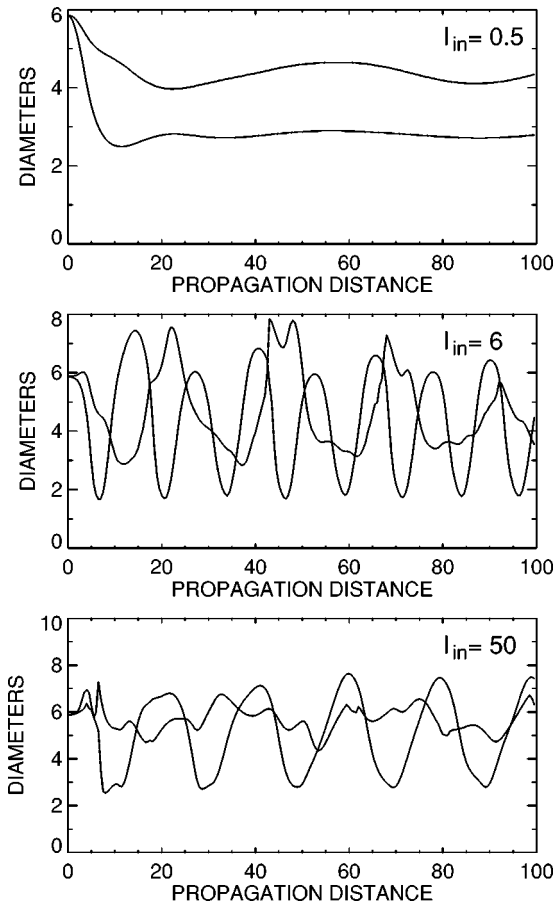

FIG. 4. Spatial evolution of diameters of an initially round Gaussian beam for $I_{\text{in}}=0.5$, 6, and 50.

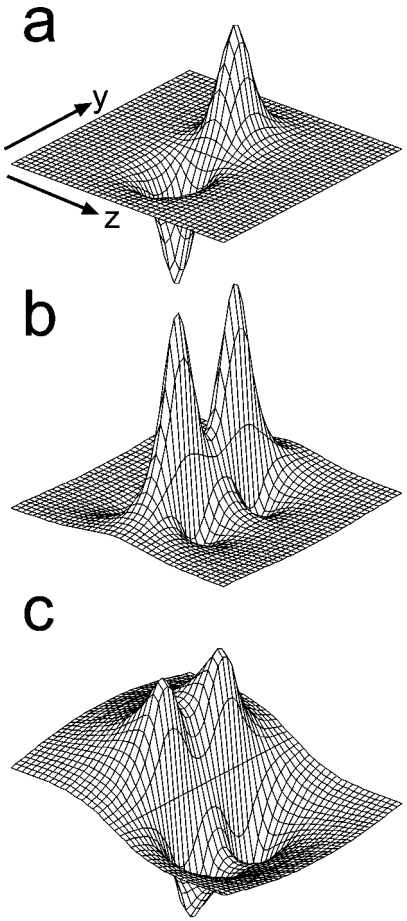

FIG. 5. Spatial distribution of the field (a), the nonlinear refractive index (b), and the induced potential (c) for the dipole solitary solution of Eqs. (2).

decreases the period of the oscillations, while still keeping them reasonably heavily damped thereby decreasing the length of the spatial transient. The initially round beam becomes elliptical and converges to the soliton solution as was confirmed experimentally in Ref. [15]. Further increase in I_m up to several units still decreases the spatial period of oscillations, but also sharply decreases the relaxation rate and increases the spatial transient length. In the very high saturation regime the oscillation period starts to grow, and the relaxation rate remains small, so the spatial transient length remains large. The characteristic period of oscillations in this case may exceed the length of the medium. By adjusting input parameters the output profiles of the beam in the high-saturation transient regime can be made to have a broad range of shapes starting from beams that are more elongated along the y axis to those elongated along the z axis, and including round output beams in between.

Figure 4 shows spatial evolution of the input Gaussian beam

$$B_{\text{in}}=\sqrt{I_{\text{in}}}\,\exp[-2\ln 2(r/d)^2] \tag{16}$$

for $I_{\text{in}}=0.5$, 6, and 50. In all cases the beam experiences self-focusing inside the medium. Nevertheless the character of its spatial evolution is dramatically different for different values of the saturation. Note rapid relaxation to the soliton solution in the moderate saturation regime for $I_{\text{in}}=0.5$ (after the spatial transient the beam intensity becomes approximately equal to 1.1). Note also the absence of any practical convergence to the soliton solution in the high-saturation regime. It should be mentioned that the longitudinal span of Fig. 4 considerably exceeds the characteristic lengths of photorefractive media.

IV. BOUND DIPOLE PAIRS

To find dipole solitary solutions of Eqs. (2), starter functions were specified as a pair of Gaussian beams with a π mutual phase shift spaced some distance apart. Figure 5 illustrates a typical distribution of the electromagnetic fields corresponding to the dipole solitary wave solution of Eqs. (2) (a), the corresponding distribution of the nonlinear refractive index $\nu=\partial\varphi/\partial z$ (b), and the induced potential φ (c) for the maximum intensity of the solution $I_m=1$. The solution is a pair of elliptical coupled $(2+1)$D beams that are spaced some distance apart. The pair is aligned along the y axis. The fields of each of the components comprising the pair have the same magnitude but different signs. The total field b is antisymmetric in y and symmetric in z. The intensity $|b|^2$ is symmetric both with respect to y and z, so the potential φ that is due to the source term proportional to the z derivative of the intensity is symmetric in y and antisymmetric in z.

Figure 6 shows cross sections of the electromagnetic field,

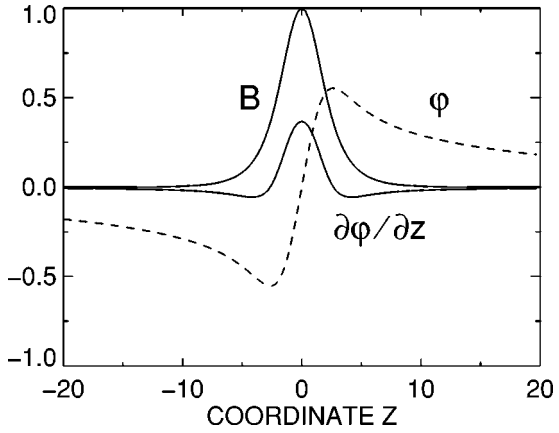

FIG. 6. Cross sections of the field, the refrative index, and the potential along the z axis through one of the maximums of the field shown in Fig. 5.

the refractive index, and the potential taken along the z axis through the maximum of one of the intensity peaks. Note the slow power-law decay of the potential at infinity.

In Fig. 7 we present the diameters d_y and d_z of each of the beams comprising the dipole solution and the separation L_{sep} between them as functions of the maximum intensity I_m. The diameters have been calculated at the $\frac{1}{2}$ level of the maximum intensity of the solution. Both of the intensity peaks comprising the dipole solution turn out to be smooth Gaussian-type beams that are narrower along the coordinate z and wider in the perpendicular direction. This structure of the beams is very similar to that of the single beam solitons discussed in Sec. III, and is indicative of the dominant role of the anisotropy in their formation.

Analogously to the single-beam solitons in the weak saturation limit $I_m \ll 1$, both the values of the diameters and the separation are inversely proportional to the square root of the maximum intensity. In the opposite limit of large saturation $I_m \gg 1$, they are logarithmically proportional to it. The power and the maximum intensity of the dipole solitary solution are monotonically growing functions of the propagation constant λ. The range of intensities in Fig. 3 is mapped to a range of propagation constants λ lying in the interval $0.02 \leqslant \lambda \leqslant 0.8$. In the unsaturated limit $\lambda \leqslant 1$ the spatial distribution of the dipole soliton pair is universal, and does not depend on the value of the propagation constant except for a rescaling. The

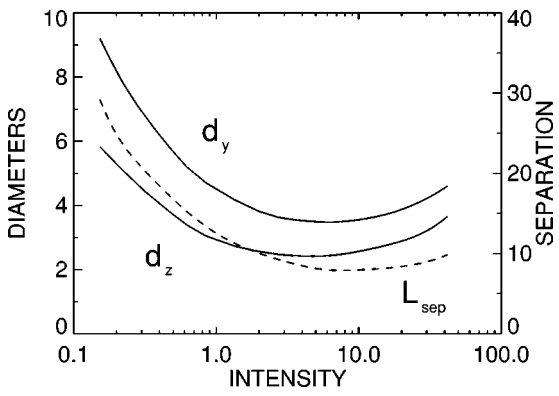

FIG. 7. Diameters and the separation between the beams comprising the dipole solitary solution vs its maximum intensity.

corresponding argumentation replicates that of Sec. III.

Numerical analysis of spatial evolution of various initial distributions of the field indicates that the dipole pairs are attractors of the set of equations (2). They are not the only attractors of the system, since Eqs. (2) also have the single beam soliton solutions discussed in Sec. III. Initial distributions of the field sufficiently close to the dipole solitary solutions converge to these solutions, as was demonstrated experimentally in Ref. [16]. As with single-beam solitons, the rate of convergence depends primarily on the normalized intensity I_m. Below we will discuss evolution of input fields consisting of an anti-phased pair of Gaussian beams separated by the distance L along the y axis. The corresponding structure of the field is of the form

$$B_{\text{in}} = \sqrt{I_{\text{in}}}\{\exp[-(y-L/2)^2/d^2 - z^2/d^2] - \exp[-(y+L/2)^2/d^2 - z^2/d^2]\}, \tag{17}$$

where I_{in} is the initial maximum intensity of each of the input beams in units of saturation intensity, and d and L are their initial diameter and separation, respectively.

The spatial dynamics of the input fields (17) are similar to those of single beams. Practically all conclusions of Sec. III are directly applicable to the dipole pairs. That is, spatial evolution of the input fields, Eq. (17), is characterized by spatial oscillations of both its diameters and the separation between the beams. In the low-saturation limit $I_m \ll 1$ these oscillations are damped, but their spatial period is large since it scales as $1/I_m$. In the high-saturation limit $I_m \gg 1$ the oscillation period is smaller, but their relaxation rate is very small, and so the spatial transient length again is large. In the moderate saturation limit $I_m \approx 1$ the oscillations are still reasonably heavily damped, and the length of the spatial transient is minimized.

Figure 8 shows the spatial evolution of an input field given by Eq. (17) for two different values of the saturation intensity. Figure 8(a) corresponds to the strong-saturation regime when the input intensity is about ten times larger than the saturation intensity; Fig. 8(b) is the moderate-saturation regime with $I_m \approx 2.5$. Both figures demonstrate that two beams comprising the initial dipole form a bound pair. The rate of convergence to the dipole solitary solutions though is a strong function of the normalized light intensity. Note the rapid relaxation to the soliton solution for $I_{\text{in}} = 0.5$, and a very long transient in the high-saturation regime. Observation of the dipole solitary solutions in the high-saturation regime is problematic because of long spatial transients. On the other hand, for $I_{\text{in}} \approx 1$ the spatial transients at the output from the crystal are largely gone, and the beam is close to its asymptotic soliton shape.

V. LOW-ORDER FILAMENTATION

A. Theory

Gaussian beams lying outside the basin of attraction of the above soliton solutions exhibit complex spatial dynamics. For large beams, an order of magnitude or more wider than the soliton solutions, filamentation occurs, resulting in a

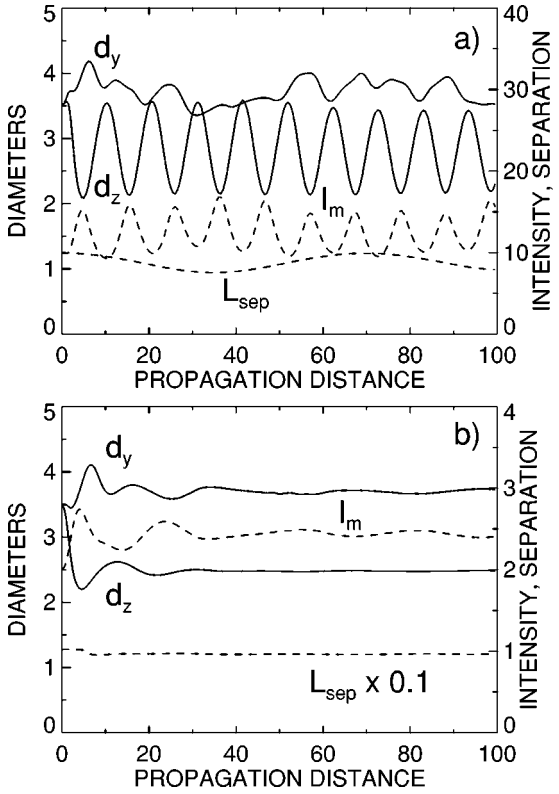

FIG. 8. Diameters, maximum intensity, and separation between peaks as functions of the propagation distance in high (a) and moderate (b) saturation regimes.

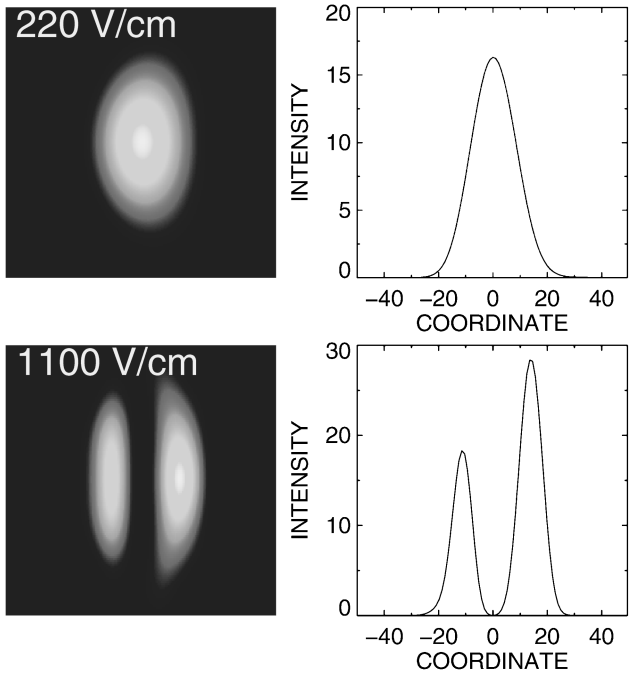

FIG. 9. Theoretical output intensity distributions of an input Gaussian beam demonstrating asymmetric beam splitting.

spatially disordered, statistically homogeneous distribution [18]. For Gaussian-type beams there are two parameters that determine the subsequent dynamics: the beam diameter and its normalized intensity. Convergence to solitary solutions is only achieved when both of these parameters start relatively close to their asymptotic values. Beams outside of the basin of attraction filament and split into several child beams that then exhibit complex oscillations of their relative sizes and energies. Depending on the initial parameters the splitting may occur along both the z and y coordinates. We refer to this as low-order filamentation. In the range of parameters considered here, where the beams start out relatively close to the basin of attraction of the solitary solutions, the dynamics are dominated by the interaction of only a few filaments. The spatial evolution is complex, and not statistically homogeneous. The interaction of several filaments in media with a cubic nonlinearity was also studied recently in Ref. [36].

The spatial dynamics of filamentation are in a first approximation well described by Eqs. (2). In particular, these equations predict correctly the splitting. A more detailed analysis reveals, however, that a noticeable experimental feature of the splitting is that there is an asymmetric exchange of energy between beamlets separated along the z coordinate. This asymmetry lies outside the behavior described by Eqs. (2) that are symmetric with respect to inversion along z. In order to account for the observed behavior we need to use the more general set of Eqs. (1).

Results of the numerical solution of Eqs. (1) demonstrating asymmetric beam splitting are shown in Fig. 9. The input boundary conditions correspond to a 34-μm Gaussian beam with the waist coinciding with the input face of the medium. The length of the medium is $l=1$ cm, the inital intensity $I_m=10$, the relevant component of the electro-optic tensor $r_{33}=360$ pm/V, the value of the characteristic internal field $\tilde{E}=700$ V/cm, and $\hat{\epsilon}_{yy}/\hat{\epsilon}_{zz}=0.5$. For zero applied field $E_{\text{ext}}=0$ the output beam remains practically round with the output diameter equal to 49 μm. The upper left frame in Fig. 9 shows the output intensity of the beam for the applied field equal to $E_{\text{ext}}=220$ V/cm, and the upper right frame shows a cross section of the intensity through the maximum along the horizontal (z) axis. The lower left frame shows the output beam intensity for $E_{\text{ext}}=1100$ V/cm, and the lower right frame is its cross section along the horizontal axis. It demonstrates the clearly asymmetric splitting of the beam at higher values of the applied field. Calculations in the $\zeta=0$ limit also give splitting, but the intensities of the split beams are equal. Calculations conducted for still wider beams show that each of the split beams may undergo secondary splittings.

Due to the presence of asymmetric terms in the material response the beam bends in the (x,z) plane when it propagates through the nonlinear medium. The center of the beam is displaced along the horizontal axis to the left by about 5 μm for $E_{\text{ext}}=220$ V/cm, and by about 26 μm for $E_{\text{ext}}=1100$ V/cm (the shift for zero applied field equals 2.8 μm). The output windows in Fig. 9 are shifted by those amounts so that the intensities are centered in their respective windows.

It is interesting to note that the intensity of the left beamlet in Fig. 9 for $E_{\text{ext}}=1100$ V/cm is smaller than that of the right one, i.e., the energy is transferred ''upstream,'' opposite to the direction of bending. This result is counterintuitive since for wide beams in the absence of an applied field the beamlets propagating to the left of the main beam gain energy, resulting in the appearance of a fan of light, moving to the left.

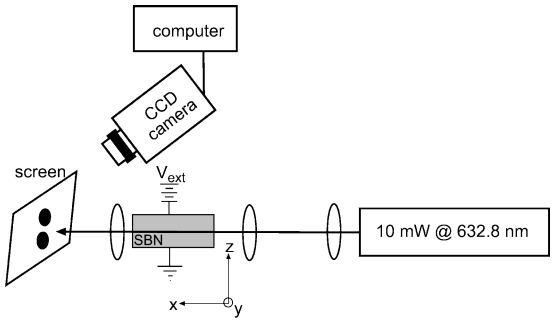

FIG. 10. Experimental setup.

B. Experiment

The experimental arrangement is shown in Fig. 10. A 10-mW He-Ne laser beam ($\lambda = 0.63\ \mu$m) was passed through a variable beam splitter and a system of lenses controlling the size of the beam waist. The beam was directed into a photorefractive crystal of SBN:60 doped with 0.002% by weight Ce. The beam propagated perpendicular to the crystal $\hat{c}$ axis, and was polarized along it to take advantage of the largest component of the electro-optic tensor of SBN r_{33}. The crystal measured 10 mm along the direction of propagation, and was 9 mm wide along the $\hat{c}$ axis. A variable dc voltage V_{ext} was applied along the $\hat{c}$ axis to control the value of nonlinear coupling. The beam intensity distributions at the output face of the crystal were imaged onto a screen and recorded with a CCD camera. The pictures were recorded after all temporal transients had died away.

The effective saturation intensity was varied by illuminating the crystal from above with incoherent white light. The dependence of the photorefractive coupling constant on saturation intensity I_d in the absence of an applied field takes the form [37] $\gamma = \gamma_0 I_{\text{beam}}/(I_{\text{beam}} + I_d)$. By measuring the two-beam coupling gain with the white light source off ($I_d = 0$) and on ($I_d \neq 0$), the ratio $I_m = I_{\text{beam}}/I_d$ was determined. These measurements have a relatively large uncertainty due to the influence of several factors, including the intensity profile of the beams, and background-stimulated scattering in the medium. The experimental uncertainty in the value of the saturation intensity is therefore larger than the uncertainty in the values of the beam diameter, externally applied field, and electro-optic coefficient, which can all be determined relatively precisely.

Experimental results demonstrating both the existence of the single solitons and convergence to them were given in Ref. [15]. Here we present a digest of those results for the reader's convenience. Figure 11 shows the output diameters of a round input 26-μm-diameter beam as functions of the applied voltage in the high-saturation regime. The insets show the beam profiles at 0.5 and 0.9 kV. Figure 12 shows the output diameters versus the applied voltage for the same beam as in Fig. 12 but, with 12 times smaller power. The inset is the output intensity distribution for 1.0-kV external voltage. In both figures, squares are experimental results and solid curves are theoretical calculations.

Figure 11 confirms the theoretical predictions of Sec. III that in the high-saturation regime the round input beam does not reach a soliton asymptotic state. Its output shape changes as a function of the voltage, the input diameter of the beam,

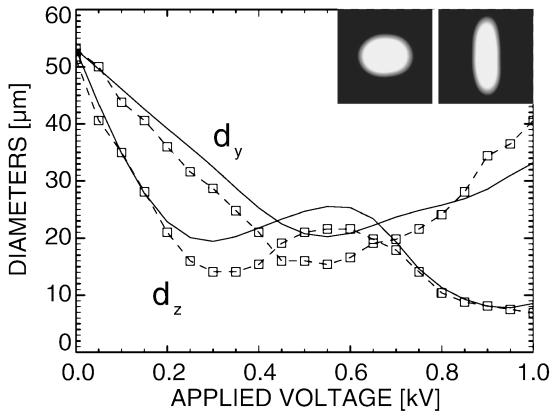

FIG. 11. Oscillatory self-focusing of a circular input beam in the high-saturation regime. The power of the input beam was 50 μW.

and the focusing conditions (we have observed ellipticities d_y/d_z ranging from about 0.5 to 5, including round output beams). Figure 12, obtained for moderate saturation intensities, demonstrates quite different behavior. That is, the output beam profile converges rapidly to an elliptically shaped soliton solution elongated along the y axis, in agreement with the theoretical results. Experimental results demonstrating existence of the dipole solitons analyzed in Sec. IV, and convergence to them were given in Ref. [16].

Below we would like to address the question of evolution of Gaussian beams lying further away in the parameter space, so that the solitons are not formed. The spatial evolution in this case is given by Figs. 13, 14, and 15 that show the change in the output intensity distribution as the applied field is increased for three different values of the saturation intensity.

Figure 13 obtained for $I_m \approx 9.5$ shows self-focusing to an elliptically shaped beam squeezed along z for $V_{\text{ext}} = 200$ V, and squeezed along y for $V_{\text{ext}} = 550$ V. Similar pictures of oscillatory self-focusing in the high saturation regime were given in Ref. [15]. Increasing the applied voltage further results in the formation of a large asymmetric bright region ($V_{\text{ext}} = 800$ V) that then splits along z into two filaments ($V_{\text{ext}} = 1050$ V). There is an asymmetric exchange of energy between the filaments, leading eventually to a strong filament

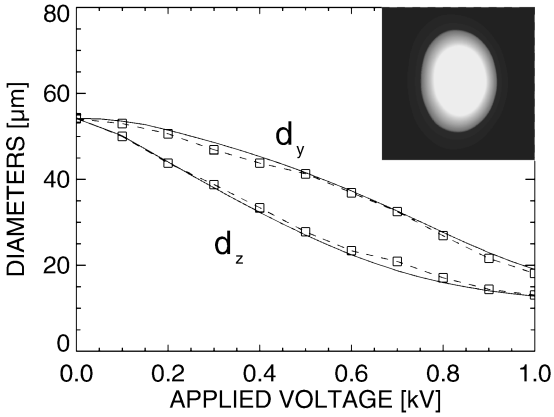

FIG. 12. Output diameters vs applied voltage for a circular input beam in the moderate-saturation regime. The power of the input beam was 4.2 μW.

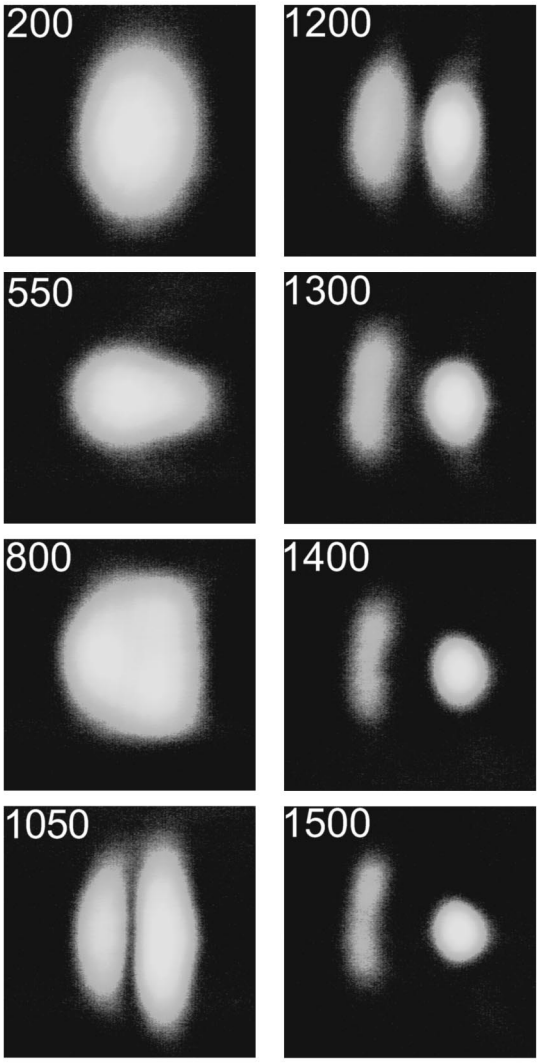

FIG. 13. Output intensity distribution vs applied voltage for $I_m \approx 9.5$. The power of the input beam was 31 μW, and its diameter was 34-μm full width at half maximum. The individual frames each depict a 100×100 μm^2 region and the z axis is horizontal.

to the right, separated several diameters from a crescent-shaped region with lower intensity to the left. The asymmetric exchange of energy along z resulted in the displacement of the beams to the left so that, as in the calculations in Sec. V A, the frames have been translated to keep the displayed filaments centered in the windows.

Comparison with Fig. 9 shows good agreement with the numerical results. In particular, the counterintuitive result that the upstream filament has a higher intensity is observed. The full width at half maximum diameter of the output beam along the z axis measured from the experimental frames $V_{\text{ext}} = 200$ and 1050 V in Fig. 13 equal 22 and 29.5 μm, respectively. In the latter case the beam is double humped, so the diameter corresponds to the width of the whole structure. The above values of the applied voltage correspond to the electric field $E_{\text{ext}} = 222$ and 1167 V/cm, given the 9-mm width of the crystal and assuming no losses at the electrodes. The theorectical diameters in Fig. 9 are equal to 19.5 μm for $E_{\text{ext}} = 220$ V/cm, and 30 μm for $E_{\text{ext}} = 1100$ V/cm, using the measured value of $r_{33} = 360$ pm/V. The intensity minimum between the peaks is more pronounced on the theoretical figure than on the experimental one. Additional comparisons with other frames show that in general the experimental and theoretical results agree to within 20% error. Note also that additional measurements and calculations using a 20-mm-long crystal with $r_{33} = 210$ pm/V showed no evidence of splitting.

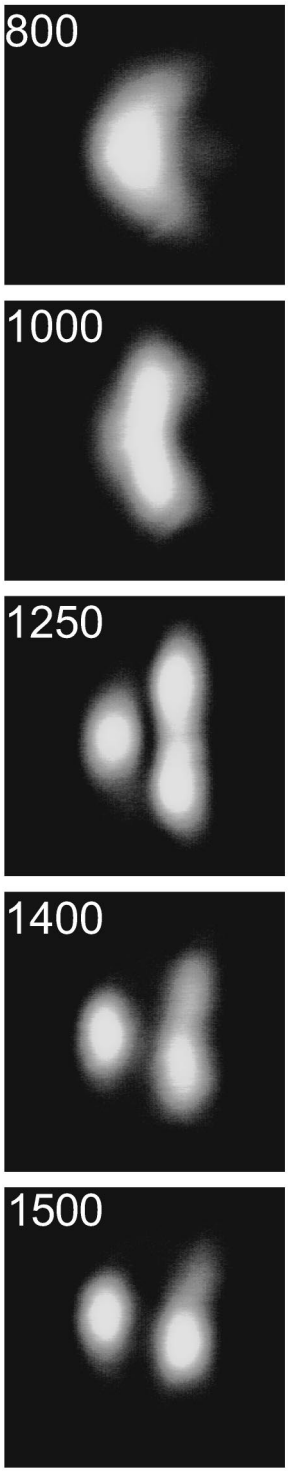

FIG. 14. Output intensity distribution vs applied voltage for $I_m \approx 6$. All other parameters are the same as in Fig. 13.

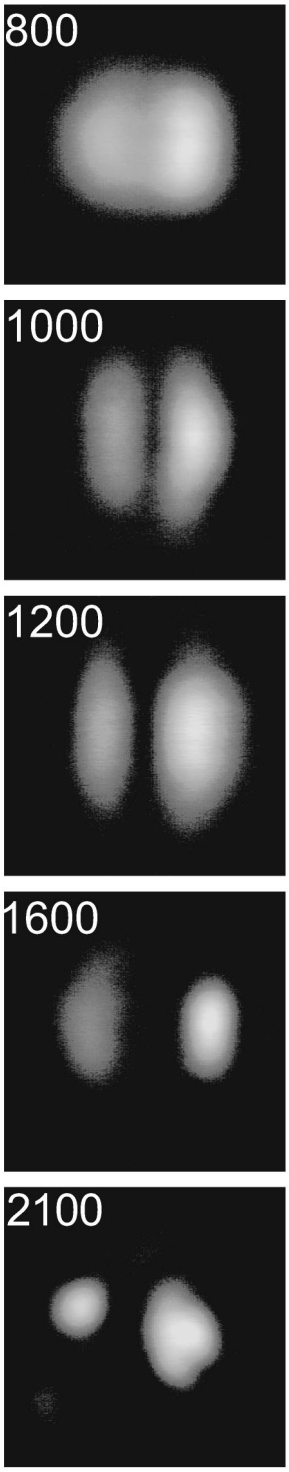

FIG. 15. Output intensity distribution vs applied voltage for $I_m \approx 19$. All other parameters are the same as in Fig. 13.

The output intensity distributions for lower and higher values of the saturation are shown in Figs. 14 and 15. In all cases the most prominent feature is asymmetric splitting along the z coordinate with most of the energy captured by the filament on the right. In Fig. 14 there is also a further splitting along the y axis. This may be understood qualitatively as follows. When the beam is very much larger than the characteristic scale of an individual filament, it breaks up into many filaments [18]. The characteristic size of a filament is smaller in Fig. 14 than in Fig. 13, since the saturation is smaller (see Fig. 1). The increased ratio of beam size to filament size in Fig. 14 is sufficient to allow splitting along the y coordinate. It is not surprising that splitting occurs more easily along z due to the fact that the nonlinearity is stronger by order 50% along z than along y [26].

The effect of varying the saturation for fixed external voltage is shown in Fig. 16. The first four frames show the output beam for $I_m \approx 0.5$ to $I_m \approx 2.2$. In this range of parameters the length of the spatial transient is still reasonably short so that these frames demonstrate convergence or near convergence to solitary solutions. In agreement with Fig. 1 the beam diameters for $I_m \approx 2$ are noticeably less than for $I_m \approx 0.5$. For intermediate values of the saturation ($I_m \approx 3.5$ to $I_m \approx 32$) the output beams are elongated along y, and split along the z coordinate. At very high values of saturation there is no splitting, and we see an elliptical output beam squeezed along either y or z. In this parameter regime the spatial evolution along x is characterized by large oscillations of the diameters (see Fig. 4), so that the shape of the output beam, for a given length of nonlinear medium, depends on the particular value of the saturation parameter.

VI. DISCUSSION

In this paper we presented a detailed analysis of $(2+1)$D soliton solutions in media with a photorefractive nonlinearity, and addressed the question of convergence to these solutions. Our results demonstrate that the rate of convergence is dramatically different for different values of the saturation (rapid relaxation to the soliton solution in the moderate saturation regime, and the absence of any practical convergence to the soliton solution in the high-saturation regime). Dependence of the character of the spatial evolution on the value of the saturation is not specific to the $(2+1)$D case, and pertains equally well to the $(1+1)$D limit. In this limit ($\partial/\partial y = 0$) the photorefractive nonlinearity (for $\zeta = 0$) is identical to the saturable Kerr nonlinearity, and Eqs. (2) reduce to

$$\left[\frac{\partial}{\partial x} - \frac{i}{2}\frac{\partial^2}{\partial z^2}\right] B(x,z) = i\frac{|B|^2}{1+|B|^2} B. \tag{18}$$

Soliton solutions of Eq. (18) were analyzed in Ref. [38].

Figure 17(a) shows the spatial evolution of the diameter of the input Gaussian beam $B_{\rm in} = \sqrt{I_{\rm in}} \exp[-2 \ln 2 (z/d)^2]$ in the $(1+1)$D case for $I_{\rm in} = 0.5$ (solid), 5 (dotted), and 50 (dashed curve). The similarities between this figure and the $(2+1)$D case (Fig. 4) are evident. Figure 17 confirms the convergence of an arbitrary beam to its asymptotic soliton shape in the moderate saturation regime ($I \approx 1$). It also demonstrates that the only way to observe solitons experimentally in a photorefractive medium in the strong saturation regime ($I \gg 1$) is to start from those solitons. The most common choice of input beam in experiments is a Gaussian beam. A Gaussian profile does not match the exact soliton shape, but in the $(1+1)$D case it is possible to adjust the diameter of this input beam so that it is close to a soliton. This is illustrated by Fig. 17(b), that shows the spatial evolution of a Gaussian beam with input diameter equal to 4.2 and $I_{\rm in} = 50$ (the dashed line). The input diameter was chosen to ensure the minimum possible deviations from the soliton

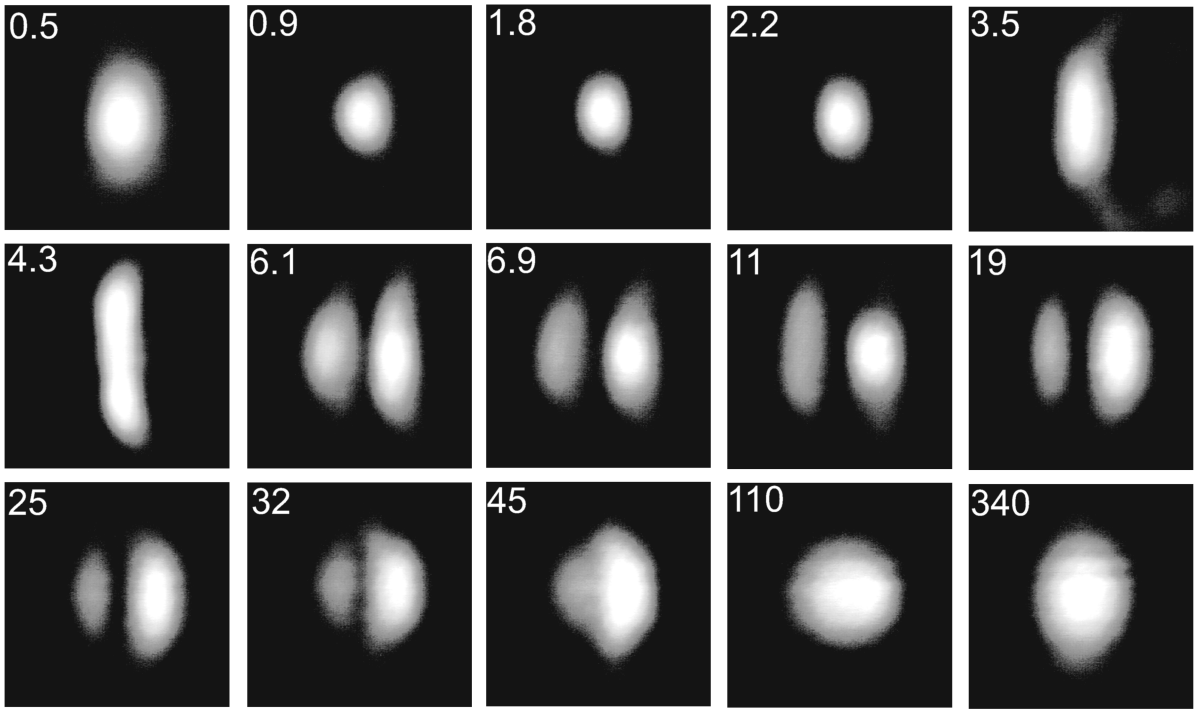

FIG. 16. Output intensity distribution vs saturation parameter for $V_{\text{ext}}=1250$ V. The frames are labeled with the value of I_m, and all other parameters are the same as in Fig. 13.

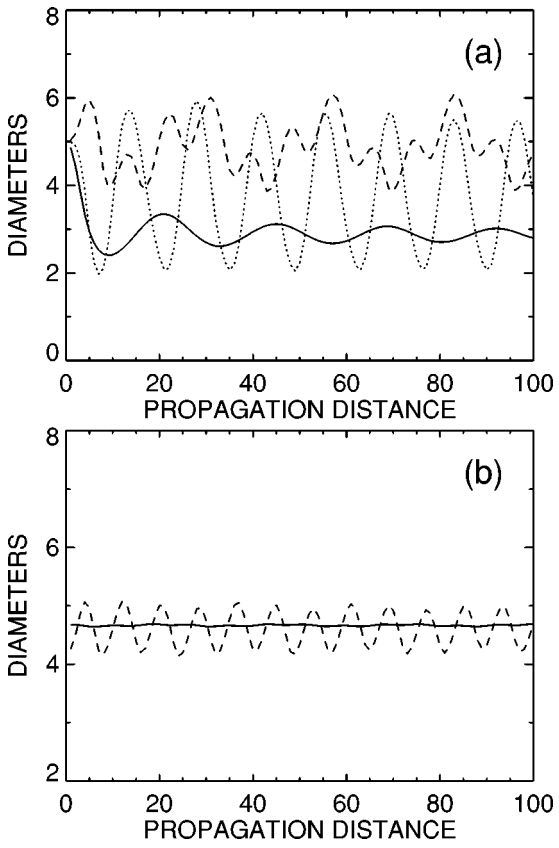

FIG. 17. Evolution of the diameter of an input Gaussian beam in the $(1+1)$D case for $I_{\text{in}}=0.5$ (solid), 5 (dotted), and 50 (dashed line) (a); evolution of the ''best-matched'' input Gaussian with $d=4.2$ and $I_{\text{in}}=50$ (dashed) and the soliton solution (solid line) (b).

solution (solid line). From a rigorous point of view, an experimental observation of the soliton in the high saturation regime is questionable even with this fitting of the input Gaussian profile to a soliton shape. Since deviations from the soliton shape do not decay [see Fig. 17(a)], it can be argued that the beam remains an oscillating Gaussian, exhibiting no trend of convergence toward a soliton. From the practical point of view the above argument may be unimportant, since the beam remains sufficiently close to a soliton solution.

The situation is qualitatively different in the $(2+1)$D case. Any radially symmetric beam ($d_y/d_z=1$) differs significantly from an elliptic soliton solution ($d_y/d_z\approx 1.5$), and no adjustments of its diameter will make it close. Besides specifying input soliton profiles, the only practical possibility to observe $(2+1)$D soliton solutions experimentally in a photorefractive medium is to work in the moderate saturation regime where the intensity of the beam is about the saturation intensity.

Another point worth mentioning is that, strictly speaking, the soliton solutions found above are only valid for $\zeta=0$. For any finite value of ζ, propagation through a sufficiently long medium results in a bending of the beam trajectory toward the direction of the applied field. Thus, in a strict sense, within the framework of Eqs. (1), there are no solitary solutions that propagate along x. In practice, for finite nonlinear media, such solutions coexist adiabatically with a slow bending of the trajectory in the direction of the applied field. The trajectory bending has been mentioned above in Sec. V. The slow bending is not of paramount experimental concern, since the longest photorefractive crystal used for soliton experiments to date is the approximately 20-mm-long sample used here and in Refs. [16,19]. The amount of bending at

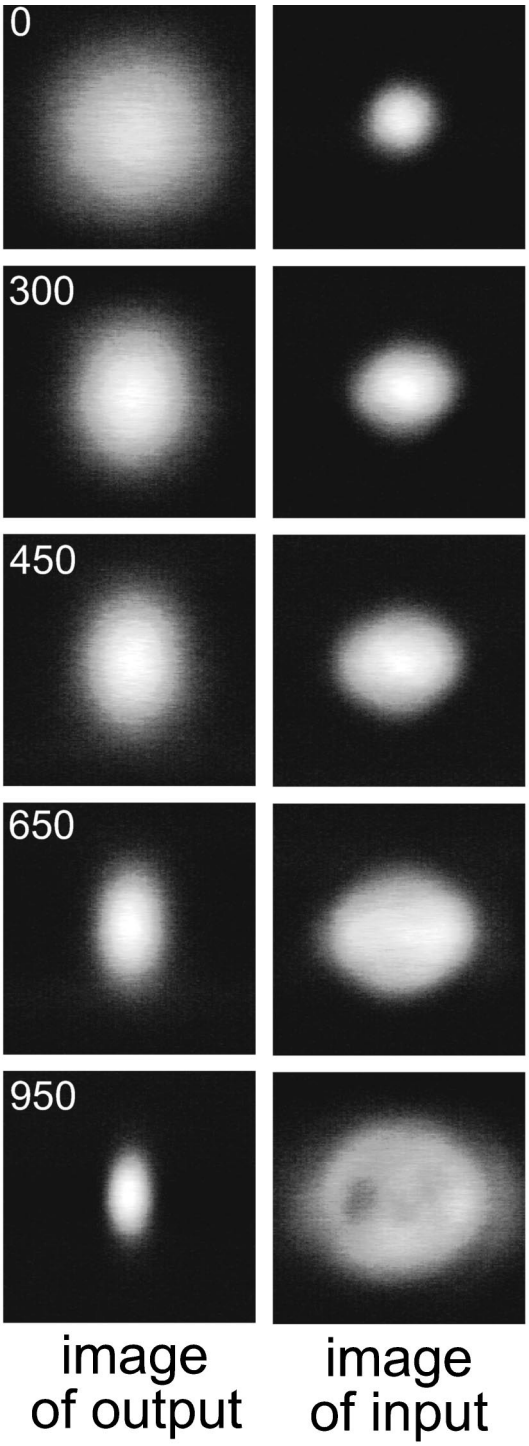

FIG. 18. The result of imaging through an inhomogeneous waveguide. Each row is labeled with the value of the applied voltage.

such distances is relatively small.

Photorefractive self-focusing is essentially anisotropic [26,27]. The spatial shape of soliton solutions is determined uniquely by the anisotropy, as discussed above. Some previous reports of soliton formation in photorefractive media have claimed to observe both circular and elliptical solitons squeezed in either transverse direction depending on the voltage [39]. In our opinion, those observations correspond to a spatially transient regime of evolution of a light beam, where such oscillations of the output diameters as a function of the voltage indeed take place (for their detailed experimental analysis, see Ref. [15]).

We note that considerable experimental care must be exercised when observing self-focusing effects. The only directly accessible information about the intensity profile of the beam is its distribution at the output face of the crystal. Attempting to measure the beam profile inside the nonlinear medium can lead to erroneous conclusions, as was pointed out in the second of Ref. [12]. Two techniques have been employed elsewhere: side-view imaging of the one-dimensional beam profile along the direction of propagation, and end-view imagng of the two-dimensional profile looking through the nonlinear medium. Side-view images of the beam profile do not correspond to the direct intensity distribution of the beam, but are due to scattering of light on inhomogeneities of the crystal. Proper interpretation of the images requires solving an inverse problem accounting for the presence of the nonlinear lens and the scatterers. We have found that images taken inside the volume of the crystal frequently are misleading. In many cases they show needle-like structures of light that might be interpreted as solitons formed in the crystal. Unfortunately their quantitative value is close to zero, since they do not allow one to measure the values of the beam diameters inside the crystal, and hence make any quantitative comparisons with the theory.

End-view images of the directly transmitted intensity distribution are not affected by the distribution of scattering inhomogeneities, but are strongly distorted by the nonlinear lens. To illustrate the errors associated with imaging through the nonlinear medium, consider Fig. 18. The figure gives a direct comparison between the output intensity distribution (left column) observed as the applied voltage is changed, and the input intensity distribution obtained by imaging through the nonlinear medium (right column). For $V_{\mathrm{ext}}=0$ the input and output images both show a circularly symmetric beam, as expected. As V_{ext} is increased the output image shows self-focusing and convergence to an elliptical soliton. On the other hand, the image of the circular input beam as obtained by looking through the nonlinear waveguide becomes elliptical and strongly distorted. Strong anisotropy of the nonlinear aberrations renders it impossible to determine even qualitatively the correct structure of the internal beam by imaging through the medium.

ACKNOWLEDGMENTS

A.A.Z. and D.Z.A. acknowledge the support of NSF Grant No. PHY90-12244 and the Optoelectronics Computing Center, an NSF Engineering Research Center. The work at Risø was supported by the Danish Natural Science Research Council.

[1] W. J. Firth and A. J. Scroggie, Phys. Rev. Lett. **76**, 1623 (1996); M. Brambilla, L. A. Lugiato, and M. Stefani, Europhys. Lett. **34**, 109 (1996); N. N. Rosanov, Prog. Opt. **XXXV**, 1 (1996).

[2] M. J. Ablowitz and H. Segur, *Solitons and the Inverse Scattering Transform* (SIAM, Philadelphia, 1981).

[3] K. Fesser, A. R. Bishop, and D. K. Campbell, Phys. Rev. B **27**, 4804 (1983).

[4] W. Krolikowski, N. Akhmediev, and B. Luther-Davies, Opt. Lett. **21**, 782 (1996); M. I. Carvalho, S. R. Singh, D. N. Christodoulides, and R. I. Joseph, Phys. Rev. E **53**, 53 (1996); Z. Chen *et al.*, Opt. Lett. **21**, 1821 (1996).

[5] S. V. Manakov, Zh. Eksp. Teor. Fiz. **65**, 505 (1973) [Sov. Phys. JETP **38**, 248 (1974)]; R. S. Tasgal and J. Potasek, J. Math. Phys. (N.Y.) **33**, 1208 (1992); J. U. Kang *et al.*, Phys. Rev. Lett. **76**, 3699 (1996).

[6] L. A. Abramyan and Yu. A. Stepanyants, Zh. Eksp. Teor. Fiz. **88**, 1616 (1985) [Sov. Phys. JETP **61**, 963 (1985)].

[7] Yu. B. Gadidei, K. Ø. Rasmussen, and P. L. Christiansen, Phys. Lett. A **203**, 175 (1995).

[8] J. S. Hesthaven *et al.*, Phys. Fluids **7**, 2220 (1995).

[9] H. A. Haus, Appl. Phys. Lett. **8**, 128 (1966); Z. K. Yankauskas, Izv. Vyssh. Ucheb. Zaved. Radiofiz. **9**, 412 (1966) [Sov. Radiophys. **9**, 261 (1966)].

[10] J. M. Soto-Crespo, D. R. Heatley, E. M. Wright, and N. N. Akhmediev, Phys. Rev. A **44**, 636 (1991).

[11] G. L. Alfimov *et al.*, Phys. Lett. A **138**, 443 (1989); Physica D **44**, 168 (1990).

[12] M. D. Iturbe-Castillo *et al.*, Appl. Phys. Lett. **64**, 408 (1994); Opt. Commun. **118**, 515 (1995).

[13] G. C. Duree, Jr. *et al.*, Phys. Rev. Lett. **71**, 533 (1993); **74**, 1978 (1995); M. Taya, M. C. Bashaw, M. M. Fejer, M. Segev, and G. C. Valley, Phys. Rev. A **52**, 3095 (1995).

[14] M. Chauvet *et al.*, Opt. Lett. **21**, 1333 (1996); M.-F. Shih, Z. Chen, M. Segev, T. H. Coskun, and D. N. Christodoulides, Appl. Phys. Lett. **69**, 4151 (1996); C. M. Gómez Sarabia, P. A. Marquez Aguilar, J. J. Sánchez Mondragón, S. Stepanov, and V. Vysloukh, J. Opt. Soc. Am. B **13**, 2767 (1996); W. Królikowski, N. Akhmediev, B. Luther-Davies, and M. Cronin-Golomb, Phys. Rev. E **54**, 5761 (1996); G. Montemezzani and P. Günter, Opt. Lett. **22**, 451 (1997).

[15] A. A. Zozulya, D. Z. Anderson, A. V. Mamaev, and M. Saffman, Europhys. Lett. **36**, 419 (1996).

[16] A. V. Mamaev, A. A. Zozulya, V. K. Mezentsev, D. Z. Anderson, and M. Saffman, Phys. Rev. A (to be published).

[17] M. D. Iturbe-Castillo *et al.*, Opt. Lett. **20**, 1853 (1995).

[18] A. V. Mamaev, M. Saffman, D. Z. Anderson, and A. A. Zozulya, Phys. Rev. A **54**, 870 (1996).

[19] A. V. Mamaev, M. Saffman, and A. A. Zozulya, Phys. Rev. Lett. **77**, 4544 (1996); **78**, 2108 (1997).

[20] S. Mallick *et al.*, J. Appl. Phys. **63**, 5660 (1988); H. C. Pedersen and P. M. Johansen, Phys. Rev. Lett. **77**, 3106 (1996).

[21] T. Honda, Opt. Lett. **18**, 598 (1993); A. V. Mamaev and M. Saffman, Europhys. Lett. **34**, 669 (1996).

[22] R. Y. Chiao, E. Garmire, and C. H. Townes, Phys. Rev. Lett. **13**, 479 (1964).

[23] J. H. Marburger, Prog. Quantum Electron. **4**, 35 (1975); M. Karlsson, Phys. Rev. A **46**, 2726 (1992); D. Suter and T. Blasberg, *ibid.* **48**, 4583 (1993); M. Dowell *et al.*, *ibid.* **52**, 3244 (1995).

[24] Y. Matsuno, Int. J. Mod. Phys. B **9**, 1985 (1995).

[25] S. V. Manakov, V. E. Zakharov, L. A. Bordag, A. R. Its, and V. B. Matveev, Phys. Lett. A **63**, 205 (1977).

[26] A. A. Zozulya and D. Z. Anderson, Phys. Rev. A **51**, 1520 (1995).

[27] N. Korneev *et al.*, J. Mod. Opt. **43**, 311 (1996).

[28] A. Davey and K. Stewartson, Proc. R. Soc. London, Ser. A **388**, 191 (1974).

[29] V. E. Zakharov, Zh. Eksp. Teor. Fiz. **62**, 1745 (1972) [Sov. Phys. JETP **35**, 908 (1972)].

[30] V. I. Bespalov and V. I. Talanov, Pis'ma Zh. Eksp. Teor. Fiz. **3**, 471 (1966) [JETP Lett. **3**, 307 (1966)]; R. Y. Chiao *et al.*, IEEE J. Quantum Electron. **2**, 467 (1966); R. G. Brewer and J. R. Lifsitz, Phys. Lett. **23**, 79 (1966); V. V. Korobkin and R. V. Serov, Pis'ma Zh. Eksp. Teor. Fiz. **6**, 642 (1967) [JETP Lett. **6**, 135 (1967)].

[31] J. Feinberg, J. Opt. Soc. Am. **72**, 46 (1982).

[32] A. A. Esayan, A. A. Zozulya, and V. T. Tikhonchuk, Kratk. Soobshch. Fiz. **5**, 45 (1990) [Sov. Phys. Lebedev. Inst. Rep. **5**, 62 (1990)].

[33] A. A. Zozulya, M. Saffman, and D. Z. Anderson, Phys. Rev. Lett. **73**, 818 (1994).

[34] V. I. Petviashvili, Fiz. Plazmy **2**, 469 (1976) [Sov. J. Plasma Phys. **2**, 257 (1976)].

[35] V. I. Petviashvili and O. A. Pokhotelov, *Solitary Waves in Plasma and in the Atmosphere* (Energoatomizdat, Moscow, 1989) (in Russian).

[36] L. Bergé, M. R. Schmidt, J. Juul Rasmussen, P. L. Christiansen, and K. Ø. Rasmussen, J. Opt. Soc. Am. B (to be published).

[37] N. V. Kukhtarev *et al.*, Ferroelectrics **22**, 949 (1979).

[38] S. Gatz and J. Herrmann, J. Opt. Soc. Am. B **8**, 2296 (1991).

[39] M.-F. Shih *et al.*, Electron. Lett. **31**, 826 (1995).